

Suppression of potential roughness in atom-chip ac Zeeman traps

S. Du, A. R. Ziltz, W. Miyahira , and S. Aubin 

Department of Physics, College of William and Mary, Williamsburg, Virginia 23187, USA



(Received 31 January 2022; accepted 18 April 2022; published 31 May 2022)

We present several toy models for predicting the character and strength of the roughness of ac Zeeman trapping potentials generated by imperfections in wire traces on an atom chip. An ac Zeeman trapping potential is generated by targeting a microwave or rf magnetic field at hyperfine or Zeeman ground-state transitions, respectively, while a dc Zeeman trap uses a static magnetic field to manipulate an atom via its magnetic moment. We find that an ac Zeeman trap suppresses potential roughness by several orders of magnitude with respect to a comparable dc Zeeman trap. This suppression stems from the inherent differences between an atom's response to dc and ac (namely rf and microwave) magnetic fields, in concert with how the ac skin effect smooths out a current distribution disturbed by a conductivity variation. For chip wires fabricated by evaporation, we find that an ac Zeeman trap for ^{87}Rb atoms, located $100\text{ }\mu\text{m}$ from the chip and operating on a 6.8 GHz hyperfine transition, is expected to suppress potential roughness by a factor of 4×10^5 compared with a similar dc Zeeman trap. For a comparable ac Zeeman trap operating on a 10 MHz Zeeman transition, the suppression is 2×10^4 . Conversely, the ac skin effect also slightly exacerbates potential roughness, in ac Zeeman traps, from defects in the sidewall of a wire trace.

DOI: [10.1103/PhysRevA.105.053127](https://doi.org/10.1103/PhysRevA.105.053127)

I. INTRODUCTION

Atom chips offer experimenters a miniaturized, low-power, scalable platform for producing ultracold atomic gases, while also providing precision control and integration of magnetic, electric, rf, microwave, and even optical fields [1]. Precision photolithography, developed by the semiconductor industry, enables the production of complicated wire layouts that can be used to sculpt complex magnetic fields for trapping and manipulating cold atoms. Atom chips have been successfully used to produce Bose-Einstein condensates (BECs) [2] and degenerate Fermi gases [3], one-dimensional (1D) gases [4], atom interferometers [5–7], and to study atom-surface interactions [8]. Due to all of these favorable properties, commercial cold atom apparatuses use atom chips, including the cold atom apparatus on the International Space Station [9]. Atom chips are also a favored platform for atomtronics, in which ultracold atoms are manipulated in circuit-like structures [10].

Despite all of these benefits, atom chips have not been widely adopted by experimenters, in part due to the roughness in the magnetic trapping potential that manifests itself primarily at very low temperatures (i.e., at the onset of BEC), or when the trap is brought close to a chip wire [11]. This roughness limits several key functions: strong confinement in 1D potentials [11], propagation of a BEC through a trapping waveguide [12], and atom interferometry [5,13]. The use of evaporation deposition to manufacture high-quality atom-chip traces has helped to reduce the degree of roughness [14]. However, small variations in the bulk conductivity of a trace still lead to enough roughness that atoms are typically trapped at chip distances of more than $100\text{ }\mu\text{m}$ with amp-scale currents. Notably, an oscillating trapping field (kHz range) can suppress roughness by generating a smoother time-averaged potential [15] but requires a more complicated apparatus.

Recently, graphene has been proposed as a two-dimensional (2D) wire material for reducing roughness [16].

At present, atom chips use the dc Zeeman (DCZ) effect to generate a magnetostatic potential, but the ac Zeeman (ACZ) effect offers an alternate on-chip approach for trapping atoms. The ACZ effect generates a spin state-specific energy shift, i.e., a potential, when a rf or microwave magnetic field drives one of the atom's ground-state Zeeman or hyperfine transitions near resonance [17,18]. Recently, ACZ potentials based on rf near fields on an atom chip have been used to trap atoms [19]. Furthermore, rf and microwave near fields on atom chips have been used to translate and manipulate atoms in a spin-specific manner [7,20,21]. ACZ potentials generate a force with an ac field gradient and are a subset of a broader class of rf and microwave dressed potentials [22,23]. This paper does not consider rf or microwave adiabatic potentials, which primarily generate a force with a dc magnetic gradient and use an ac field to couple spin states [6].

In this paper, we show theoretically that an ACZ chip trap should substantially suppress potential roughness due to localized conductivity variations in an atom-chip wire, with respect to its DCZ counterpart. This suppression is due both to the physics of the ACZ effect for our trapping geometry and the tendency of the current in a chip wire to hug its edges at rf frequencies and higher (ac skin effect). The skin effect also leads to somewhat larger potential roughness from wire edge defects, although this increase is relatively small.

The paper is structured in the following manner: Section II introduces the basic theory of DCZ and ACZ chip traps. In Sec. III, we explain the roughness suppression mechanism in a chip-based ACZ trap. Section IV presents a thin wire model for current defects and compares the roughness of ACZ and DCZ traps. In Sec. V, we study roughness suppression and

enhancement versus microwave frequency due to the ac skin effect. We conclude in Sec. VI with a summary of the results and an outlook for future research.

II. ATOM-CHIP TRAPS

In this section, we present the basic physics and equations for calculating the trapping potentials for DCZ and ACZ traps generated by currents in atom-chip wires. Both DCZ and ACZ potentials for an atom are described by the Zeeman interaction Hamiltonian between an atom's magnetic moment $\vec{\mu}$ and an external magnetic field \vec{B} :

$$H_{\text{Zeeman}} = -\vec{\mu} \cdot \vec{B}. \quad (1)$$

The magnetic field \vec{B} can be static or time dependent, e.g., an oscillating ac field. If we neglect the nuclear spin \vec{I} , then, for an alkali-metal atom, the magnetic moment is given by $\vec{\mu} = (2\mu_B/\hbar)\vec{S}$. Here, \vec{S} is the spin operator for the valence electron, \hbar is Planck's constant, and μ_B is the Bohr magneton.

A. dc Zeeman trap theory

At ultracold temperatures, the motion of an atom through a spatially varying static magnetic field \vec{B}_{dc} is sufficiently slow that the magnetic moment of the atom follows the direction of the local magnetic field, i.e., the angle between $\vec{\mu}$ and \vec{B}_{dc} does not change. At low magnetic-field strength, the total angular momentum of the atom $\vec{F} = \vec{I} + \vec{S}$ is a good quantum number, and m_F , the projection of \vec{F} onto the local direction of \vec{B}_{dc} , does not vary as the atom moves through the magnetic field. In this case, the dc Zeeman energy E_{DCZ} of the atom in a specific Zeeman state, m_F , is proportional to the magnitude of the local magnetic field and is given by

$$E_{\text{DCZ}} = m_F g_F \mu_B |\vec{B}_{dc}| \quad (2)$$

where g_F is the Landé g factor [24]. E_{DCZ} represents both a shift in the energy of the atom's internal state and the potential energy of the atom in the magnetic field. As Earnshaw's theorem prevents the existence of magnetic maxima in free space, a magnetic trap can only be used to trap “weak-field seeker” states (with $m_F g_F > 0$) at a magnetic minimum [see Fig. 1(a)].

In the case of an atom chip, a micromagnetic trap is formed at the magnetic field minimum produced at the point \vec{r}_0 where an applied external magnetic field \vec{B}_{ext} cancels the field \vec{B}_{wire} of a current carrying wire trace, as shown in Fig. 1(b). An additional uniform magnetic field \vec{B}_{Ioffe} , directed along the z axis of the wire trace, ensures that the magnetic field minimum (at the trap bottom) is nonzero. If \vec{B}_{ext} is sufficiently uniform, then the magnetic field is quadrupolar in the vicinity of the trap bottom and harmonic in the magnitude (at lowest order):

$$\vec{B}_{dc}(x, y) \simeq \frac{B_{\text{wire}}}{h} (\Delta y \hat{x} + \Delta x \hat{y}) + B_{\text{Ioffe}} \hat{z}, \quad (3)$$

$$B_{dc}(x, y) \simeq B_{\text{Ioffe}} + \frac{B_{\text{wire}}(\vec{r}_0)^2}{2h^2 B_{\text{Ioffe}}} (\Delta x^2 + \Delta y^2), \quad (4)$$

where Δx and Δy represent position with respect to the trap minimum, and h is the distance from the wire to the trap minimum in the xy plane. In the case of a thin infinite wire, the distance is $h = \mu_0 I_{dc} / 2\pi B_{\text{ext}}$, where I_{dc} is the current in the

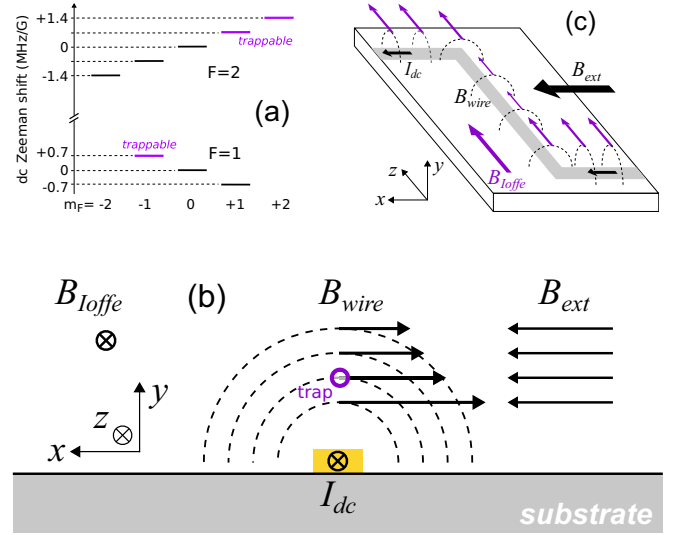


FIG. 1. Basic physics of a DCZ micromagnetic chip trap. (a) Plot of the dc Zeeman energy shift E_{DCZ} for different m_F states in the $F = 1$ and $F = 2$ hyperfine manifolds of an alkali-metal atom with nuclear spin $I = 3/2$, e.g., ^7Li , ^{23}Na , $^{39,41}\text{K}$, ^{87}Rb . Only the states whose dc Zeeman shift is positive can be trapped, i.e., they are weak-field seekers. (b) A trap is formed at the magnetic minimum where the magnetic field B_{wire} , generated by the chip wire current I_{wire} , is canceled by an opposing uniform magnetic field B_{ext} . An additional magnetic field B_{Ioffe} directed along the current axis lifts the magnetic zero at the trap to a finite value. (c) B_{Ioffe} is provided by an externally applied uniform magnetic field directed along the \hat{z} direction (large purple arrow) and the endcap wires of the Z-shaped wire (gray). The field from the endcaps (smaller purple arrows) is strongest at the ends of the central wire, thus providing trapping along the z axis.

wire, and μ_0 is the permeability of free space. Equation (4) gives an approximate expression for the field magnitude, which provides the harmonic radial confinement in the xy plane.

Axial confinement. Confinement along the axial direction (z axis) is typically provided by “endcap” wire segments to form a Z-shaped wire [see Fig. 1(c)]. The current in the transverse endcap segments generates a z -axis component to the magnetic field that adds locally to B_{Ioffe} , so that $B_{\text{Ioffe}}(z)$ is larger at either ends of the central wire segment, thus providing axial confinement. As we see later (Sec. III), spurious transverse currents within the central portion of the “Z” wire can generate unwanted localized axial confinement, i.e., potential roughness, in DCZ chip traps.

B. ac Zeeman trap theory

The ACZ effect is generated by the same Zeeman Hamiltonian [Eq. (1)] as the DCZ effect. In the most basic implementation, two Zeeman states $|g\rangle$ and $|e\rangle$ (in the atom's ground state) experience an ACZ energy shift, when an ac magnetic field \vec{B}_{ac} drives an allowed $M1$ transition between these two states [see Fig. 2(a)]. Similar to the ac Stark effect, the ACZ energy shift is a resonant effect, and its strength depends strongly on the detuning $\delta = \omega_{\text{ac}} - \omega_{\text{eg}}$ between the driving frequency ω_{ac} and the bare transition frequency ω_{eg} . Furthermore, the ACZ effect mixes the $|g\rangle$ and $|e\rangle$ states,

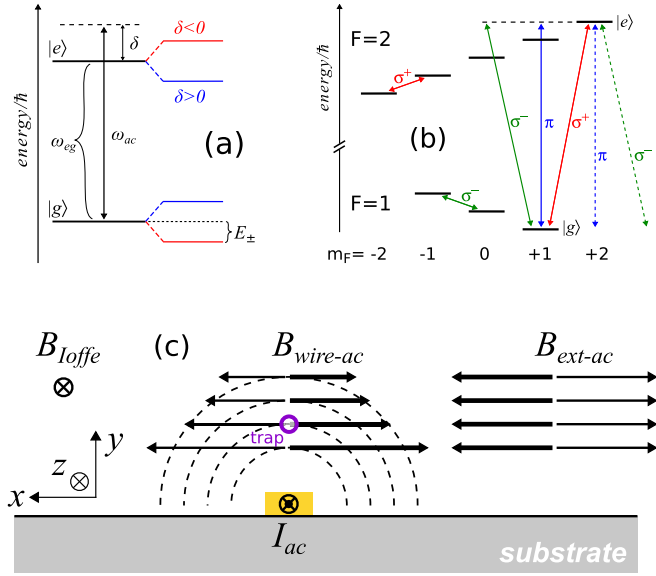


FIG. 2. Basic physics of an ac Zeeman chip trap. (a) ac Zeeman shift E_{\pm} in a two-level atom due to an ac magnetic field. Depending on the detuning δ of the driving field frequency ω_{ac} relative to the bare transition frequency ω_{eg} , the ground and excited states are either symmetrically repelled (red-detuning) or pulled together (blue-detuning). (b) ACZ transition polarization types (σ^+ , σ^- , and π) between Zeeman states in the ground level of an alkali-metal atom with nuclear spin $I = 3/2$. The $|g\rangle$ - and $|e\rangle$ -labeled states form an effective two-level system, if the dc Zeeman shift between neighboring states is sufficiently large. (c) A trap is formed at the ac magnetic field zero where the ac magnetic field $B_{\text{wire-ac}}$, generated by the chip wire current I_{ac} , is canceled by an in-syn opposing uniform magnetic field $B_{\text{ext-ac}}$ at the same ac frequency. B_{loffe} is a dc magnetic field, applied along the wire's z axis, which provides a dc Zeeman shift to separate the Zeeman states within the $F = 1$ and $F = 2$ hyperfine manifolds.

which results in new eigenstates for the system, $|+\rangle$ and $|-\rangle$ (i.e., the “dressed states”), with the following eigenenergies [17,25]:

$$E_{\pm} = \pm \frac{\hbar}{2} (-|\delta| + \sqrt{\delta^2 + |\Omega|^2}) \quad (5)$$

where $\Omega = \langle g | -\vec{\mu} \cdot \vec{B}_{ac} | e \rangle / \hbar$ is the Rabi frequency for the interaction between the atom and the ac magnetic field.

As we will see later, the far-detuned limit, with $|\delta| \gg |\Omega|$, is a case that is typical in an ACZ trap. In this limit, the $|g\rangle$ and $|e\rangle$ barely mix, and they can be identified with the $|\pm\rangle$ eigenstates. In this case, the ACZ energy shift is similar to that of the ac Stark shift, and Eq. (5) becomes $E_{g,e} = \pm \hbar |\Omega|^2 / 4\delta$, with $+$ for $|g\rangle$ and $-$ for $|e\rangle$. The state mixing decreases significantly with increased detuning: the probability for the atom to be found in the other state is $P_{\text{other}} = |\Omega|^2 / 4\delta^2$.

The Rabi frequency Ω is determined by the interaction geometry of the ac magnetic field and the atomic spin. In a circular polarization basis with a quantization axis along the \hat{z} direction, the Rabi frequency can be written as [25]

$$\Omega = -\frac{\mu_B}{\hbar^2} \langle g | S_+ B_{ac,-} + S_- B_{ac,+} + 2S_z B_{ac,z} | e \rangle, \quad (6)$$

where $S_{\pm} = S_x \pm iS_y$ are the spin raising and lowering operators and $B_{ac,\pm} = B_{ac,x} \pm iB_{ac,y}$. The matrix elements in Eq. (6)

can be calculated once the $|g\rangle$ and $|e\rangle$ states are identified with specific $|F, m_F\rangle$ states. Notably, at low magnetic-field strength, angular momentum selection rules require that a circularly polarized ac magnetic field $B_{ac,\pm}$ (and for \vec{B}_{ac} along \hat{x} and \hat{y}) can only drive σ^{\pm} transitions such that $\Delta m_F = \pm 1$. For \vec{B}_{ac} parallel to the z axis, π transitions are allowed such that $\Delta m_F = 0$. Exact expressions for calculating the Rabi frequency Ω in the low dc magnetic-field limit are given in Ref. [25].

Polarization selectivity. Figure 2(b) shows that often only a single polarization component of the ac driving field (i.e., equivalent to σ^+ , σ^- , or π type) will affect the ACZ energy shift of a $|F, m_F\rangle$ spin state, due to angular momentum selection rules and transition detunings. For example, in the case of microwave hyperfine transitions, e.g., between the $F = 1$ and $F = 2$ hyperfine manifolds at 6.8 GHz for ^{87}Rb , the $|e\rangle = |F = 2, m_F = 2\rangle$ state can only experience an ACZ shift via a σ^+ transition with the $|g\rangle = |F = 1, m_F = 1\rangle$ state. The same is true for the $|g\rangle$ state over a narrow range of driving field frequencies, i.e., if the transitions of $|g\rangle$ to the $|F = 2, m_F = 1\rangle$ and $|F = 2, m_F = 0\rangle$ states are sufficiently off-resonance. In this case, the $|g\rangle$ and $|e\rangle$ states form an effective two-level system over a narrow range of driving frequencies or if the drive field is purely left-circularly polarized.

In the case of rf Zeeman transitions between m_F states within a hyperfine manifold, only a single polarization component is involved. Atoms in the $F = 1$ ($F = 2$) manifold can only undergo σ^- (σ^+) Zeeman transitions and are thus only affected by the right-circularly (left-circularly) polarized component of a rf driving magnetic field. So far, we have used a microwave hyperfine transition [i.e., $|e\rangle \leftrightarrow |g\rangle$ in Fig. 2(b)] to illustrate ACZ trapping physics, but the nearly degenerate rf Zeeman transitions within each hyperfine manifold can be used to form an ACZ trap as well: the ACZ physics is similar, and Eq. (5) is qualitatively correct [19,21].

ACZ trapping scheme. A rf ACZ chip trap has recently been demonstrated [19] and borrows many elements of a DCZ chip trap. Figure 2(c) shows the ACZ trap architecture that this paper will use to compare the roughness of ACZ and DCZ trapping potentials. An ac current I_{ac} in a wire along the z axis generates an ac magnetic near field $\vec{B}_{\text{wire-ac}}$, while an external ac magnetic field $B_{\text{ext-ac}}$ is oriented parallel to the chip surface along the x axis. The relative phase of $B_{\text{wire-ac}}$ and $B_{\text{ext-ac}}$ is chosen so that these fields always oppose each other and cancel at a point \vec{r}_0 to form the local field minimum for the trap, which is located at a distance $h = \mu_0 I_{ac} / 2\pi B_{\text{ext-ac}}$ directly above the wire. Small shifts in the relative phase between $B_{\text{wire-ac}}$ and $B_{\text{ext-ac}}$ will result in small horizontal shifts in the trap location (along $\pm \hat{x}$) [25], so the phase must be stabilized to prevent position jitter and associated heating. In practice, for rf frequencies, a roughly uniform $B_{\text{ext-ac}}$ can be generated by two additional parallel chip wires on either side of the central wire shown in Fig. 2(c) [26]. For operation at microwave frequencies, microstrip transmission lines can be used in place of the wires (see Sec. V) [25]. Finally, a uniform dc magnetic field B_{loffe} applied along the z axis (parallel to wire) separates the Zeeman state energies and provides a convenient quantization axis. We note that with this arrangement of fields, $B_{\text{wire-ac}}$ and $B_{\text{ext-ac}}$ can only drive σ^{\pm} transitions.

Finally, as long as h is much smaller than the wavelength $\lambda_{ac} = 2\pi c/\omega_{ac}$ (c is the speed of light), then $\vec{B}_{wire-ac}$ can be treated as a near field, i.e., it is given by its static form times an oscillatory ac term: $\vec{B}_{wire-ac} = \vec{B}_{wire} \exp(i\omega_{ac}t)$. In this case, the magnetic near field obeys Earnshaw's theorem, and so the chip can only generate an ac magnetic field minimum: an ACZ chip trap can only confine weak-field seekers, i.e., spin eigenstates that experience a positive ACZ energy shift. Notably, since the atoms are trapped in a region of low ac magnetic field, with $B_{ac} = 0$ and $\Omega = 0$ at the trap bottom, sufficiently cold atoms will be confined in the far-detuned limit with $|\delta| \gg |\Omega|$. If atoms are warm enough, then they can climb the potential and experience a larger field and Ω . Setting $|\delta| = |\Omega|$ in Eq. (5), we can see that the trapped atoms will be in the far-detuned limit so long as their temperature is much less than $T \simeq 0.21\hbar|\delta|/k$ (k is Boltzmann's constant). For example, for a detuning $|\delta| = 2\pi \times 1$ MHz, the atoms will be trapped in the far-detuned limit for temperatures well below $T \simeq 10$ μ K and thus will be largely in a single one of the $|F, m_F\rangle$ spin states.

Both the DCZ and ACZ chip traps tend to produce harmonic potentials at the bottom of the traps. Figure 3 shows the trapping potentials for similar ACZ and DCZ traps: both traps are located at $h = 100$ μ m above the chip wire and have a transverse trapping frequency $\omega_r = 2\pi \times 1$ kHz for the $|2, 2\rangle$ ground state of ^{87}Rb . While the potentials at the bottom of each trap are identical, they differ away from the bottom and have significantly different trap depths. However, in this paper, we focus only on the potential roughness in the vicinity of the trap bottom.

Axial confinement. While adding endcap wires or deforming the ends of the wire can generate some axial confinement for an ACZ trap, this effect is not as large as in a DCZ trap, since the atoms are much less sensitive to π polarized microwaves or rf. One alternative is to generate a standing wave, or *microwave lattice*, by directing additional microwaves of the same frequency and amplitude from either end of the trapping wire: If these microwaves are at a different detuning from the transverse confinement microwaves, then they will not affect the transverse trapping, but they will provide axial confinement. Conveniently, the phase of the standing wave controls the longitudinal position of the trap.

III. ACZ ROUGHNESS SUPPRESSION

In a DCZ chip trap, potential roughness originates from deviations of the current I_{dc} from the straight path of the wire. As shown in Fig. 4(a), a local variation in wire resistivity (conductivity patch) or a defect in the side wall of a wire trace (edge defect) can cause a local deviation in the average current direction. Improvements in atom-chip manufacturing, notably the use of evaporation deposition, have reduced these deviations and in particular edge defects. At present, the scale for local deviations of a wire trace edge is 100 nm. However, local resistivity variations persist and typically give rise to current deviations on the order of 0.1 mrad over distances on the order of 100 μ m. These deviations are much larger than those generated by edge defects and are the primary source of potential roughness. Table I summarizes the current deviation

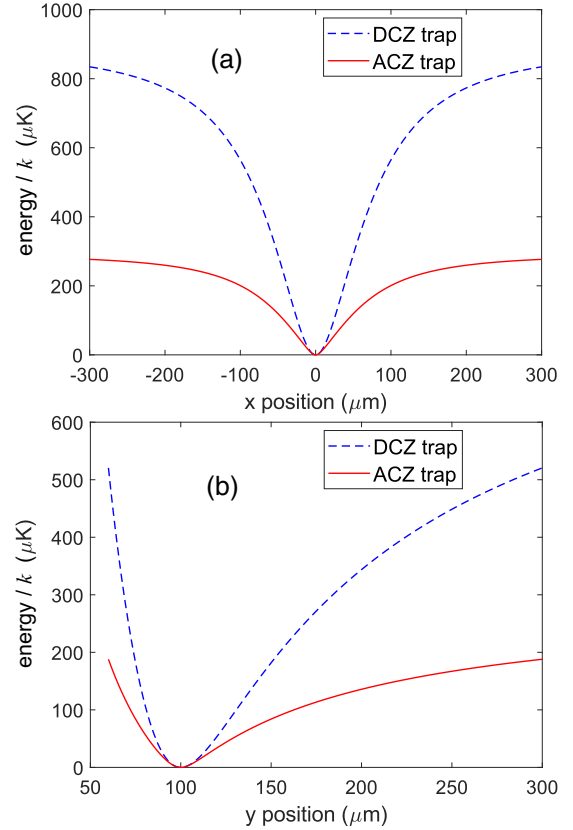


FIG. 3. Comparison of similar ACZ and DCZ chip traps. Both traps have a transverse harmonic trapping frequency of $\omega_r = 2\pi \times 1$ kHz for the $|2, 2\rangle$ ground state of ^{87}Rb and are located at $h = 100$ μ m directly above the current-carrying wire in the configurations of Figs. 1(b) and 2(c). The DCZ trap uses $I_{dc} = 0.8796$ A, $B_{ext} = 17.592$ G, and $B_{loffe} = 5$ G. The trap bottom of the DCZ trap has been set at 0 μ K, i.e., the energy offset from B_{loffe} has been subtracted. The ACZ trap operates on the $|2, 2\rangle \leftrightarrow |1, 1\rangle$ hyperfine transition of ^{87}Rb at $\omega_{ac} = 2\pi \times 6.8$ GHz and uses $I_{ac} = 0.543$ A (0.384 A rms), $B_{ext-ac} = 10.86$ G, and detuning $\delta = 2\pi \times 1$ MHz; B_{loffe} is not specified since it does not affect the trap (as long as the associated DCZ shifts are much larger than δ). (a) Trapping potentials versus x for $y = 100$ μ m. (b) Trapping potentials versus y for $x = 0$ μ m.

parameters and wire defects reported for some atom chips based on evaporation deposition.

The current deviation in a DCZ chip trap generates potential roughness by modifying the axial magnetic field (along the z axis). If the current deviates by an angle θ away from the current propagation direction \hat{z} [see Fig. 4(b)], then the magnetic field \vec{B}_{wire} that it generates will now include a longitudinal component $B_{||} = B_{wire} \sin \theta$ along \hat{z} . Importantly, this $B_{||}$ component adds linearly to B_{loffe} . In the small-angle limit, the current deviation makes a contribution $B_{wire}\theta$ to B_{loffe} and thus to the potential energy at the bottom of trap [see Eq. (4)]. In contrast, the deviation reduces only slightly the B_{\perp} component of \vec{B}_{wire} along the x axis by $B_{wire}\theta^2/2$. In the DCZ trapping potential of Fig. 3, a very long 0.1 mrad deviation ($l/2 \gg h$) will generate a potential bump or valley on the order of 100 nK, which is of the same order as the BEC transition temperature. The blue curve in Fig. 5 shows the

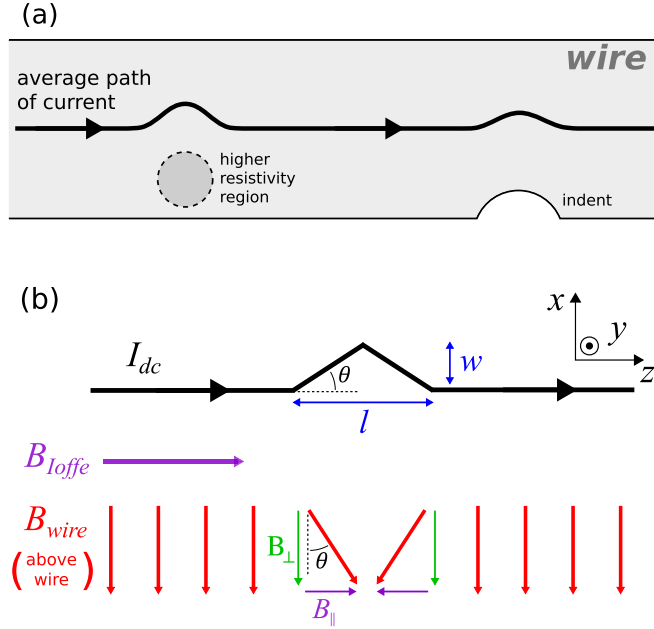


FIG. 4. Current path due to defects in a wire. (a) Illustration of the average path of the current in a planar wire trace due a local variation in resistivity (conductivity patch defect) and an indentation in the wire border (edge defect). (b) 1D current model for a wire trace defect and corresponding magnetic field. A wire defect causes a “bump” deviation of the dc current I_{dc} (black) from a straight line trajectory by an angle θ . The bump has an amplitude w and a length l . The current generates a magnetic field B_{wire} (red) perpendicular to the current, while the current bump results in a magnetic-field component $B_{||}$ parallel to the current direction, which adds locally to B_{loffe} (purple). In the case of an ac current I_{ac} , all of the magnetic fields are ac except B_{loffe} .

longitudinal potential-energy profile at the original location of the trap bottom for a DCZ chip trap with the same parameters as Fig. 3 and for the triangular current deviation shown in Fig. 4(b) with $\theta = 0.1$ mrad and $l = 100$ μm : The positive (negative) angle of the deviation generates the potential bump (valley).

In the case of an ACZ chip trap, the longitudinal ac deviation component $B_{||} \simeq B_{wire-ac}\theta$ (along \hat{z}) cannot contribute to

TABLE I. Summary of typical current-bump deviation dimensions and wire trace defect parameters for atom chips fabricated by evaporation deposition.

Defect parameter	Representative value	Range
Grain size	90 nm	30–70 nm [27,28] 100 nm [29], <100 nm [11] 70 nm [30]
Edge defect	100 nm	<100 nm [29], 100 nm [11,31]
Bump angle θ	0.1 mrad	0.04–0.16 mrad rms [27] 0.1–0.4 mrad pk-pk [27] <0.1 mrad [11]
Bump length l	100 μm	10–50, 79, 90, 300 μm [27]

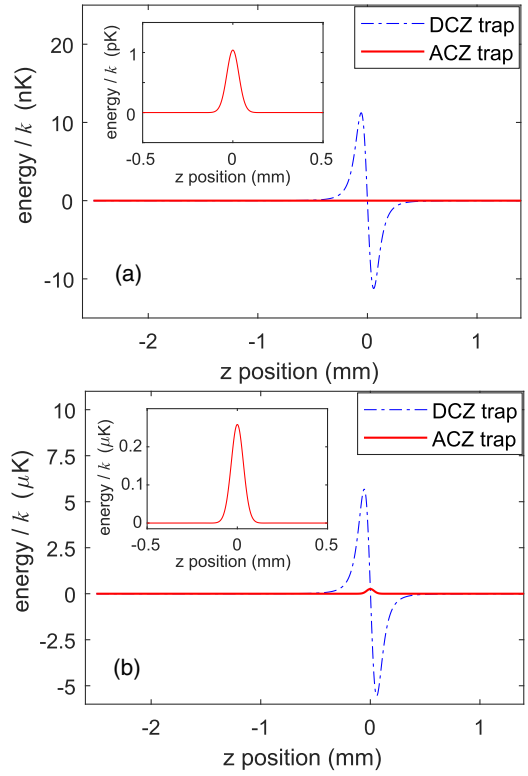


FIG. 5. ACZ and DCZ potential distortion at the original trap location due to a single current deviation located at $z = 0$. The potential distortion is plotted versus axial position z along the wire trace. (a) Potential distortion from a small current deviation based on Table I: current bump with $w = 5$ nm, $l = 100$ μm , and $\theta = 0.1$ mrad. The inset shows a zoom-in on the much smaller ACZ potential perturbation. (b) Potential distortion due to a large current deviation: current bump with $w = 2.5$ μm , $l = 100$ μm , and $\theta = 50$ mrad. The inset shows a zoom-in on the ACZ potential perturbation. The potential distortions are based on calculations described in Sec. IV for the same ACZ and DCZ traps used for Fig. 3.

B_{loffe} , which remains a dc field. Instead, $B_{||}$ can only contribute to the ACZ potential by driving a π transition with angular momentum selection rule $\Delta m_F = 0$. As the trap operates on σ^\pm transitions, π transitions will either be unavailable or far off-resonance, and so the $B_{||}$ component will contribute much less or not at all to the ACZ trapping potential. For example, in the energy-level diagram of Fig. 2(b), an ACZ trap operating on the microwave σ^+ hyperfine transition for the $|e\rangle$ state has no π transition that can be spuriously driven. In the case of a similar trap for the $|g\rangle$ state, a π transition exists but is suppressed, since it is far off resonance (if B_{loffe} is sufficiently large). In the case of an ACZ trap based on rf Zeeman transitions, there are no π Zeeman transitions that can be driven by a spurious $B_{||}$ component. However, a π hyperfine transition to the other hyperfine manifold is possible, but it is very far off resonance with a detuning δ_π given by the hyperfine splitting (i.e., $\delta_\pi = 6.8$ GHz for ^{87}Rb): if the allowed π and σ^\pm transitions have comparable couplings, then the contribution to the ACZ potential from the spurious π transition is suppressed by roughly $\theta^2\delta/\delta_\pi$.

Simplified model. In the rest of the paper, we ignore the contributions of these spurious transitions to the ACZ

potential, since they are either not possible or can be made sufficiently far off resonance to be strongly suppressed. Formally, we are modeling the ACZ potential using an atom with only two states, which simplifies the treatment significantly, but also implies that the associated ACZ roughness is somewhat underestimated with respect to a real atom with many hyperfine states, e.g., ^{87}Rb with eight hyperfine ground states. However, this simplified model is exact for an alkali-metal atom with no hyperfine structure (nuclear spin $I = 0$) and only two ground states, e.g., ^{78}Rb with a single $F = 1/2$ hyperfine manifold (18 minute half-life) [32].

The reduction in the perpendicular component B_{\perp} of $B_{\text{wire-ac}}$ due to the current deviation does not significantly affect the ACZ trapping potential. At the trap location, $B_{\text{wire-ac}}$ and $B_{\text{ext-ac}}$ cancel exactly (both are along the x axis) in the case of no current deviation. With a current deviation, the \hat{x} component of the wire's near field is $B_{\text{wire-ac}}(1 - \theta^2/2)$ at the original trap location (to lowest order), and the total microwave field is then $B_{\text{wire-ac}}\theta^2/2$. The Rabi frequency Ω at the original trap location is thus proportional to $B_{\text{wire-ac}}\theta^2/2$. In the far-detuned limit ($|\delta| \gg |\Omega|$), the ACZ trapping potential E_+ is proportional to $|\Omega|^2$, so the change in E_+ is proportional to $B_{\text{wire-ac}}^2\theta^4/4$. Due to the θ^4 dependence, this contribution to the ACZ trapping potential is relatively unimportant for small θ .

The current bump also leads to a shift in the trap location along the \hat{x} direction. This trap position shift Δx is on the order of the x axis excursion w of the current, with $\Delta x \propto w$ [see Fig. 4(b)]. Thus at the original trap location, the trapping potential increases by $\Delta E = (1/2)\omega_r^2\Delta x^2$, which is proportional to w^2 , and also proportional to θ^2 for fixed bump length l (in the small-angle limit). This position shift is true for both the ACZ and DCZ traps, but this contribution to the potential roughness is the dominant one for the ACZ trap, since the axial contribution of the DCZ potential is much larger (and scales like θ). Figure 5 shows a comparison of the distortions of the DCZ and ACZ trapping potentials for two current deviations: Fig. 5(a) shows a small current deviation given by the parameters of Table I ($\theta = 0.1$ mrad, $l = 100 \mu\text{m}$, $w = 5$ nm), and Fig. 5(b) shows an unusually large current deviation ($\theta = 50$ mrad, $l = 100 \mu\text{m}$, $w = 2.5 \mu\text{m}$). Notably, the ACZ potential deviation is always positive [$E_+ > 0$ in Eq. (5)] and does not depend on the sign of θ , and so it is symmetric around the current deviation. In contrast, the DCZ potential deviation depends on the sign of θ and is antisymmetric around the current deviation.

IV. 1D WIRE MODEL

In this section, we simulate the potential roughness of comparable ACZ and DCZ chip traps based on a simple thin wire model. While the analytic description in Sec. III provides basic scalings for the roughness of ACZ and DCZ trapping potentials, a quantitative assessment of the roughness requires a numerical calculation of the magnetic near field generated by a specific current-deviation model.

For simplicity, we construct a model for the trapping potential based on 1D current segments. As shown in Fig. 4(b) the current deviation bump is modeled as a small triangular deviation in the plane of the chip (xz plane). The triangle is

symmetric (isosceles) and has base length l and transverse deviation w . The triangular deviation is also characterized by the bump angle $\theta = \tan^{-1}(2w/l)$. Unless specified otherwise, in this section we will use the values for the current-bump triangle given in Table I: $l = 100 \mu\text{m}$ and $\theta = 0.1$ mrad (with $w = 5$ nm).

We use the Biot-Savart law to calculate the magnetic near field (dc or ac) for a current segment. The total magnetic field at a given point (x, y, z) is then the sum of the fields generated by all the individual segments, e.g., four segments in the Fig. 4(b) layout. For a segment of current I starting at position (a, b, c) , with length L , and oriented at an angle θ from the z axis (in the xz plane), the magnetic field $\vec{B}(x, y, z)$ is given by

$$\vec{B} = \frac{\mu_0 I}{4\pi} \frac{1}{\tilde{x}^2 + \tilde{y}^2} (\tilde{x}\hat{y} - \tilde{y}\cos\theta\hat{x} + \tilde{y}\sin\theta\hat{z}) \times \left(\frac{\tilde{z}}{\sqrt{\tilde{x}^2 + \tilde{y}^2 + \tilde{z}^2}} + \frac{L - \tilde{z}}{\sqrt{(\tilde{x}^2 + \tilde{y}^2 + (L - \tilde{z})^2)}} \right), \quad (7)$$

where the intermediate coordinate variables \tilde{x} , \tilde{y} , and \tilde{z} are defined as

$$\tilde{x} = -(z - c)\sin\theta + (x - a)\cos\theta, \quad (8)$$

$$\tilde{y} = y - b, \quad (9)$$

$$\tilde{z} = (z - c)\cos\theta + (x - a)\sin\theta. \quad (10)$$

To study the effect of the current deviation bump, we calculate the trapping potential with and without the bump and then take the difference of the two potentials to obtain its effect. By this method, we find that the potential roughness for an ACZ trap is substantially smaller than its DCZ counterpart.

In addition, in this section, we also study the case of a string of current deviations, i.e., connected serially one after another. All of these deviation bumps are identical and in the xz plane of the chip, although we alternate the sign of the angle θ of the deviations, as shown in Fig. 8(a). Typically, in the case of multiple current bumps, an ACZ trap further suppresses the potential roughness with respect to its DCZ counterpart.

A. Single defect

In this section, we investigate the effect of a single current deviation bump, i.e., a single defect (see Fig. 4), on the trapping potential at its unperturbed location. However, the current defect also shifts the location of the trap, and so we study the trapping potential at this new location as well, including the trapping potential minimum and the trap frequency.

We examine the effect of the single current deviation bump by subtracting the “with defect” and the “no defect” trapping potentials at the “no defect” trap location (i.e., the minimum of the unperturbed potential). Figure 5(a) shows this trapping potential difference for the ACZ and DCZ traps of Fig. 3 located at $h = 100 \mu\text{m}$ directly above the chip wire. The potential difference is plotted as a function of position along the wire trace (z axis), with the defect located at $z = 0$. The current defect triangle is given by the representative values in Table I, i.e., $\theta = 0.1$ mrad, $l = 100 \mu\text{m}$, and $w = 5$ nm. The

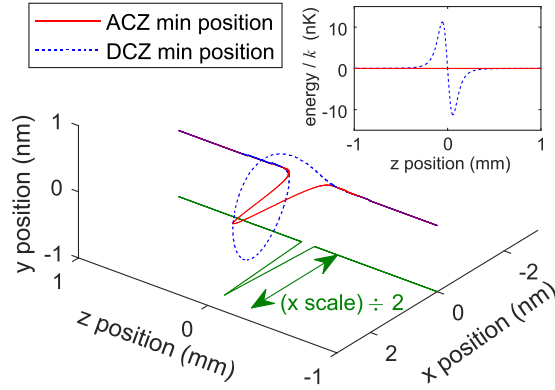


FIG. 6. Trap location deviation in 3D due to a single current-bump deviation. The unperturbed trap (same as in Fig. 3) is located along the z axis (at $x = 0, y = 0$). The wire defect is the same as in Fig. 5(a), i.e., $\theta = 0.1$ mrad, $l = 100$ μm , and $w = 5$ nm. Blue (dashed): DCZ trap bottom position. The trap deviates in both the x and y directions. Red (solid): ACZ trap bottom position. The trap only experiences a shift along the x direction. Green (solid): Current path with the x -axis scale shrunk by a factor of two for illustration purposes. In this plot, the current path is located at $y = -100$ μm position, but has been placed at $y = -1$ nm for illustration purposes. The inset shows the potential energy at the trap minimum position for the ACZ (solid red) and DCZ (dashed blue) traps. The unperturbed trap minimum energy has been subtracted.

DCZ trap experiences a bipolar potential-energy excursion of roughly ± 10 nK, while the ACZ trap experiences a much smaller potential increase of about 1 pK: The perturbation of the ACZ potential is about 10^4 times smaller than the corresponding perturbation in the DCZ potential. Figure 5(b) shows the potential perturbation for a larger current defect triangle with $\theta = 0.05$ rad, $l = 100$ μm , and $w = 2.5$ μm . In this case, the ACZ potential perturbation is only 24 times smaller than its DCZ counterpart, i.e., a 0.25 μK increase versus a ± 5.5 μK excursion. In both Figs. 5(a) and 5(b), the roughness of the ACZ trap is much smaller than for the DCZ trap. Furthermore, the ACZ potential experiences the perturbation as a positive single-sided bump, while the DCZ potential experiences the perturbation as a much larger bipolar excursion (see explanation in Sec. III).

The current deviation distorts the trapping potential sufficiently to displace the trap locally. Figure 6 shows a three-dimensional (3D) plot of the (x, y) location of the potential minimum in the xy plane as a function of axial z position, for a current deviation bump located at $z = 0$. Both the ACZ and DCZ traps experience small transverse displacements in the xy plane. The ACZ potential's (x, y) minimum is only shifted in the direction of the current bump, along the x direction: the minimum's position essentially mimics the current bump. The DCZ potential minimum is displaced in both x and y directions and traces out a spiral whose maximum x -axis displacement equals that of the ACZ potential.

The inset of Fig. 6 shows the value of the potential energy at the (x, y) minimum location as a function of the z position. The potential energy at the ACZ potential minimum along z remains at zero and is unchanged by the presence of the current bump (a zoom-in shows that it remains at zero to within the numerical error of our computations). Consequently, the

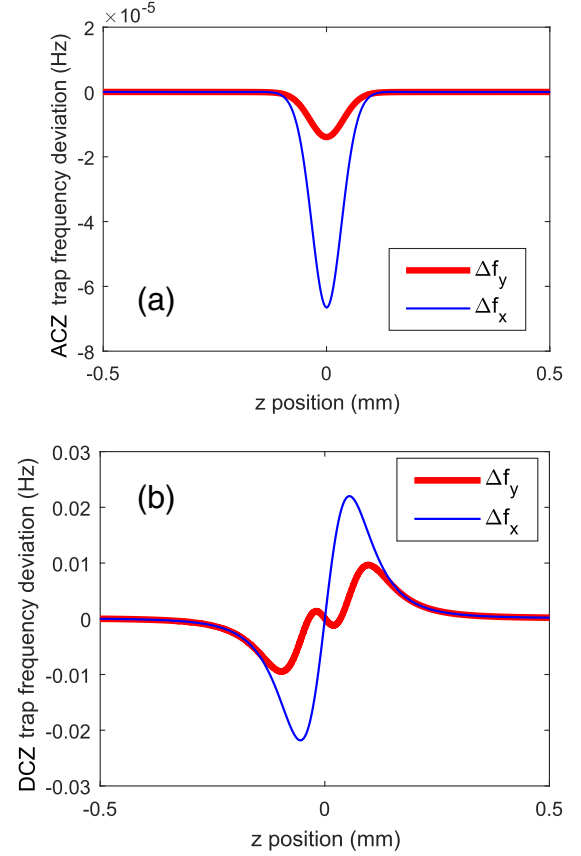


FIG. 7. Trap frequency deviations $\Delta f_{x,y}$ due to a single current bump at $z = 0$. The current bump is the same as in Figs. 5(a) and 6, i.e., $\theta = 0.1$ mrad, $l = 100$ μm , and $w = 5$ nm. The trap frequency deviation Δf for the (a) ACZ case is roughly 500 times smaller than for the (b) DCZ case. The deviation Δf is strongest along the x axis (bump direction). The unperturbed trap is the same as in Fig. 3.

current bump does not impose any axial confinement on the ACZ trap and only perturbs its layout. However, the potential energy at the DCZ potential minimum varies significantly along z over the course of its spiral path near the current bump. This variation in the potential is comparable to that in Fig. 5(a) and necessarily results in axial confinement: The result is that atoms congregate at the point with the lowest potential, generated by the current bump (i.e., just to the right of $z = 0$). This mechanism generates BEC cloud fragmentation in DCZ traps, but according to this analysis it should not occur for ACZ traps.

In addition to displacing the trap, the current deviation bump also perturbs the transverse trapping frequencies (i.e., the curvature of the trapping potential). We define the trap frequency deviation as $\Delta f = (\omega_{\text{defect}} - \omega_r)/2\pi$, where ω_r is the radial trap frequency without any current defect (i.e., $\omega_r = 2\pi \times 1$ kHz for the trap of Fig. 3) and ω_{defect} is the trap frequency with the defect. The trap frequency deviation Δf is different in the x and y directions and depends on the axial position z . Figure 7 shows the trap frequency deviations Δf_x and Δf_y as a function of axial position z for the ACZ and DCZ traps. For both traps, the change in trap frequency is quite small, although the change for the ACZ trap is three orders of magnitude smaller than for the DCZ trap. In the case of the

ACZ trap, the current bump results in a minute reduction in the trap frequencies along both transverse direction by a few tens of μHz , with the largest decrease along the x axis (bump direction). The DCZ trap experiences small bipolar changes in its transverse trap frequencies of a few tens of mHz, with the largest again along the bump direction (x axis). In both cases, the change in trap frequency is sufficiently small to have little impact (for this small current bump).

B. Multiple defects

In this section, we investigate the effect of multiple current deviation bumps on the trapping potential. In the case of a single current deviation bump, the magnetic near field is distorted beyond the immediate vicinity of the bump itself. Multiple current defects can thus be expected to contribute to the distortion of the trapping potential at a given point. Notably, we find that multiple bumps typically suppress the ACZ potential roughness but enhance the DCZ potential roughness.

We construct a model with multiple current bumps by stringing together a series of identical single bumps with alternating $\pm\theta$ deviation angles. Figure 8(a) shows a multiple-bump model with 50 current bumps. The multiple-bump model is spatially periodic with period $\lambda = 2l$ (there is no space between neighboring bumps).

In Fig. 8(b), we show the ACZ trapping potential distortion at the location of the original ACZ trap using the same bump parameters as in Fig. 5(a). Each $\pm\theta$ current bump results in alternating trap displacements in the $\pm\hat{x}$ directions of a little less than $\pm w$. The net effect is that each current bump results in a single positive ACZ trapping potential bump that is somewhat smaller in strength than a single isolated bump, e.g., as shown in Fig. 5(a). If we define the ACZ potential roughness $\Delta E_{\text{rough-ac}}$ as the peak-to-peak deviation of the distorted trapping potential in the central section of the model, then we see that $\Delta E_{\text{rough-ac}} \simeq 1$ pK in Fig. 5(a) has decreased to $\Delta E_{\text{rough-ac}} \simeq 0.5$ pK in Fig. 8(b). Furthermore, there are two ACZ potential bumps for every period λ (for a total of 50).

The DCZ trapping potential is distorted in a different manner by the presence of multiple current bumps. Figure 8(c) shows the DCZ trapping potential deviation at the location of the original DCZ trap, based on the same multibump model as Fig. 8(b). Within the series of current bumps, each angled current segment (of length l) at angle $+\theta$ generates a corresponding positive bump in the trapping potential, while segments at angle $-\theta$ generate negative dips in the potential. The net effect of the alternating $\pm\theta$ current bumps is to produce trapping potential variations that are somewhat larger in strength than a single isolated bump [see Fig. 5(a)]. The DCZ potential roughness $\Delta E_{\text{rough-dc}}$ is the peak-to-peak deviation of the distorted trapping potential in the central portion of the model: in the single bump of Fig. 5(a), $\Delta E_{\text{rough-dc}} \simeq 20$ nK, while for the multibump model of Fig. 8(c) the roughness increases to $\Delta E_{\text{rough-dc}} \simeq 30$ nK. Notably, there is only one DCZ potential bump (and dip) for every period λ (for a total of 25 bumps).

To quantify the comparison of the ACZ and DCZ trapping potential roughness, we introduce the *suppression factor*, which is the ratio of the two roughnesses for a same multiple-

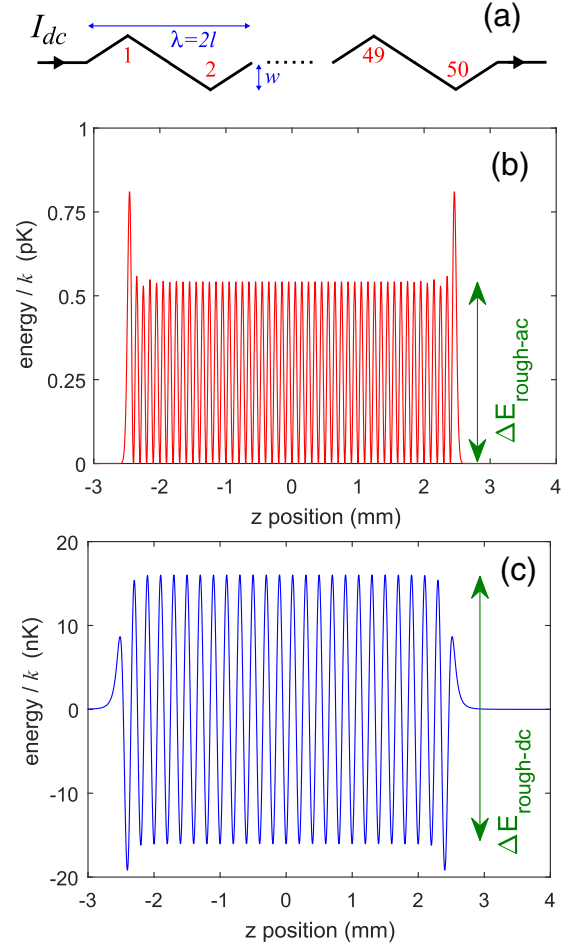


FIG. 8. Trapping potential distortion for a wire with multiple periodic current bumps. (a) Schematic of a chip wire with 50 current deviation bumps with alternating orientations (in the xy plane). The diagram is shown for a dc current I_{dc} but is identical in the case of a microwave ac current I_{ac} . The parameters for each current bump are the same as in Fig. 5(a), i.e., $\theta = \pm 0.1$ mrad, $w = \pm 5$ nm, and $l = 100$ μm . The unperturbed trap is the same as in Fig. 3. (b) Deviation of the ACZ trapping potential versus axial position z at the original trap location. (c) Deviation of the DCZ trapping potential versus z at the original trap location.

bump model:

$$\text{suppression factor} = \frac{\Delta E_{\text{rough-dc}}}{\Delta E_{\text{rough-ac}}}. \quad (11)$$

In the case of the model in Fig. 8, the suppression factor is about 6×10^4 .

We can use the suppression factor to compare how the ACZ and DCZ roughness vary relative to each other as the parameters of the multiple-bump model are varied. Figure 9 shows the suppression factor for a model with 500 current bumps as the trap height h is varied, Fig. 9(a), as the bump width w is varied, Fig. 9(b), and as the bump length l is varied, Fig. 9(c). In all three cases, the suppression factor is larger with multiple bumps than with a single current bump.

First, the magnetic roughness falls off at larger trap heights, and the ACZ roughness falls off faster than the DCZ roughness. Figure 9(a) shows that the roughness falls off faster for

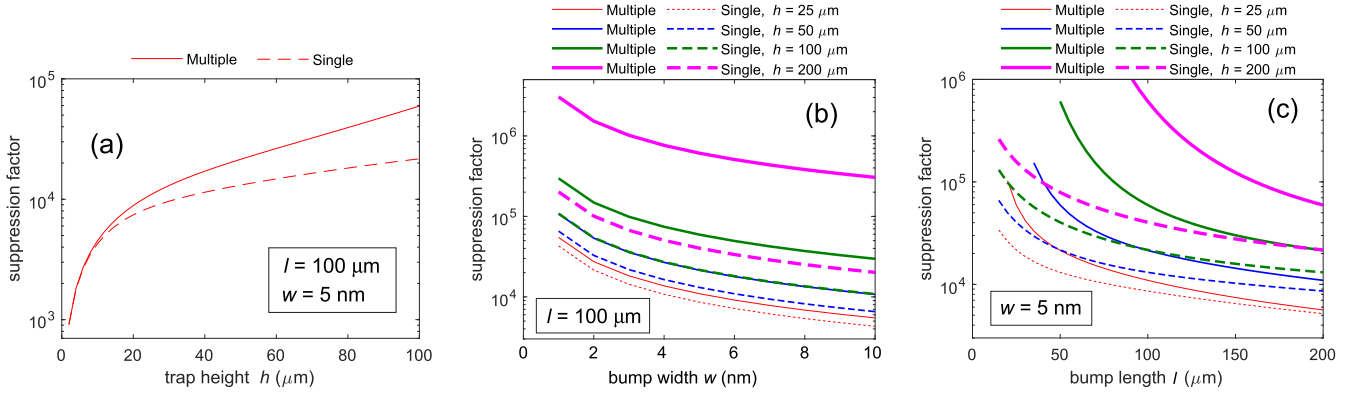


FIG. 9. Suppression factor for a wire with periodic current deviation bumps. The computations for the plots are based on the periodic current deviation model of Fig. 8 with 500 alternating current bumps. The plots show the single-bump suppression factor for comparison (dashed lines), based on the model of Fig. 4(b) with the same bump parameters as the multibump case (solid lines). The ACZ and DCZ trap frequencies are maintained at $\omega_r = 2\pi \times 1$ kHz for all of the trap heights (for all the curves in the plots). The unperturbed trap at $h = 100$ μm is the same as in Fig. 3. (a) Suppression factor versus trap height h , with bump parameters $\theta = \pm 0.1$ mrad, $w = \pm 5$ nm, and $l = 100$ μm . (b) Suppression factor versus bump width w for various trap heights; the bump length is held constant at $l = 100$ μm . (c) Suppression factor versus bump length l for various trap heights; the bump width is kept constant at $w = \pm 5$ nm.

the ACZ trap than for the DCZ trap, since the suppression factor grows quickly as the trap height h increases. Furthermore, the multiple-bump model results in somewhat more roughness suppression than the single-bump one.

Second, the suppression factor also depends on the current deviation bump width. In the case of a single bump the suppression factor is proportional to $1/wl$. This basic behavior is expected since the DCZ roughness is proportional to θ , which in the small-angle limit is given by $\theta = 2w/l$, while the ACZ roughness is proportional to w^2 and depends much less on l . Figure 9(b) shows the suppression factor as a function of current deviation width w , while keeping the deviation length fixed at $l = 100$ μm : The plot shows that the suppression factor falls off as $1/w$ in the single- and multiple-bump cases, with the latter benefiting from additional suppression of roughness.

Third, the suppression factor depends on the bump length. Figure 9(c) shows the suppression factor versus bump length l for a fixed bump width of $w = \pm 5$ nm. In the case of a single bump, the suppression factor falls off roughly as $1/l$ (at short l , the falloff is a little faster). In the case of multiple periodic current bumps, the suppression factor is again larger than the single-bump case, but also falls off faster than $1/l$, thus further suppressing short l bumps. The faster-than- $1/l$ falloff is accentuated for larger trap heights.

V. ac SKIN EFFECT

The distribution of current in a wire depends on its frequency. A dc current propagates uniformly in a wire, except for deviations due to internal wire defects, e.g., Fig. 4(a). In contrast, an ac current tends to hug the lateral edges of a trace as the frequency is increased, due to the ac skin effect [33], as shown in Fig. 10(a). While the previous section investigated differences in DCZ and ACZ potential roughnesses for a given current deviation, in this section, we study how the ac skin effect can suppress or enhance different types of current

deviations. In particular, at high frequencies, the ac skin effect strongly suppresses current deviations due to spatial conductivity variations in a wire trace. However, the ac skin effect can also somewhat exacerbate current deviations arising from defects in the edges of a wire trace.

We use a commercial electromagnetic simulation solver (FEKO by Altair, Inc.), based on the method of moments, for accurate modeling of the ac skin effect [33]. The use of such a solver also allows us to replace our simple thin wire model with a microstrip transmission line, which is a convenient building block for sculpting microwave near field structures, such as an ACZ trap [25]. Used to convey microwave signals, a microstrip is a form of transmission line consisting of a conducting trace separated from a conducting ground plane by a dielectric layer (substrate) [34]. Figure 10(a) shows a schematic of our microstrip transmission line (used for all simulations in this section) and the resulting current distribution due to the ac skin effect at 6.8 GHz. Our microstrip model has a 50 Ω impedance and consists of a 54 μm wide copper trace on a 50 - μm -thick aluminum nitride (AlN) dielectric substrate with a copper ground plane. High-frequency ac skin effect computations require a very fine discretization mesh, which in turn requires substantial computational resources, so we only use a very fine mesh over a central section of the microstrip trace's length. As shown in Fig. 10(a), the microwave current hugs the inside lateral edges of the microstrip trace.

The ac skin effect is due to the generation of eddy currents from the ac magnetic field of the microwave current, which concentrates the ac current along the skin of the conductor [33]. The skin depth characterizes the length scale for the thickness of the current “skin” and is given by $\sqrt{2/\sigma\mu\omega_{ac}}$. For example, at $\omega_{ac} = 2\pi \times 6.8$ GHz, the skin depth is 0.8 μm in copper with conductivity $\sigma = 5.813 \times 10^7$ (Ωm) $^{-1}$ and magnetic permeability $\mu \simeq \mu_0$. In the case of a ribbon-like conductor, such as the microstrip trace, the skin of the lateral current distribution is typically several skin depths wide [33].

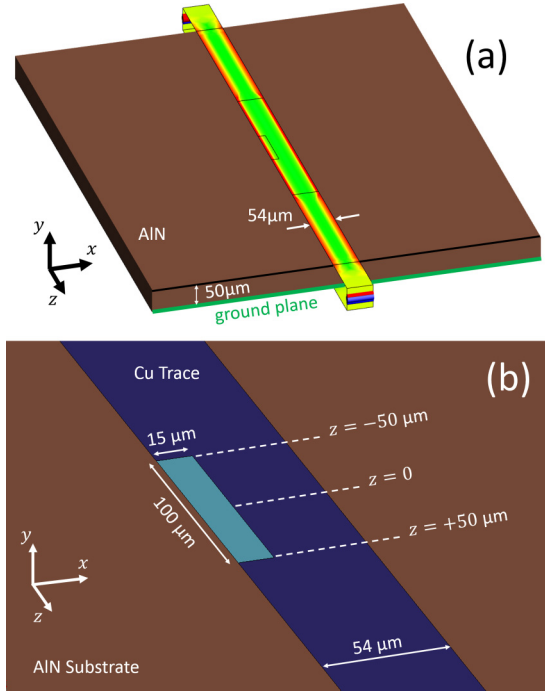


FIG. 10. Microstrip transmission line model showing the ac skin effect and the conductivity patch model. (a) Microstrip transmission line model used for all simulations in Sec. V. The copper microstrip trace is 1 mm long, 54 μm wide, and 5 μm thick and lies on a 50- μm -thick aluminum nitride (AlN) substrate with a 5- μm -thick copper ground plane. The AlN substrate has dimensions 1 mm \times 0.8 mm, dielectric constant $\epsilon = 8.9$, and a loss tangent of 0.0005. The trace uses a fine mesh with roughly 1.6 μm triangular elements (or finer) over its central 0.4-mm-long section, while the rest of the trace uses a coarser mesh with roughly 9 μm triangular elements. The current density is shown at 6.8 GHz and is only accurate in the central high-mesh section. (b) Close in view of the conductivity patch (light blue) located in the central high-mesh section of the trace (dark blue). The patch is also visible as a black rectangular outline in panel (a).

The input and output ports of the microstrip trace have 50 Ω source and load impedances, respectively, to match the broadband 50 Ω impedance of the trace (dc–20 GHz) and to suppress any standing waves. In all of the simulations presented in this section, we use a 1 V rms source, which corresponds to 20 mW of microwave power and a rms current of 20 mA. However, the roughness results in this section do not depend on the specific input power, e.g., the average transverse position of the current and fractional change in the magnetic near field are independent of the current magnitude. We compute such quantities over the range of 1 MHz to 10 GHz to determine their frequency dependence. We use 1 MHz as a stand-in for dc, since the skin depth at this frequency is larger than the trace width, resulting in a largely uniform transverse current distribution (in the absence of wire defects).

In the next two sections, we study the role of the ac skin effect in determining the current distribution, and associated magnetic roughness, in the presence of two types of defects [35]: (a) a local conductivity variation in the bulk of the microstrip trace, and (b) a small geometric defect in one of the edge walls of the trace.

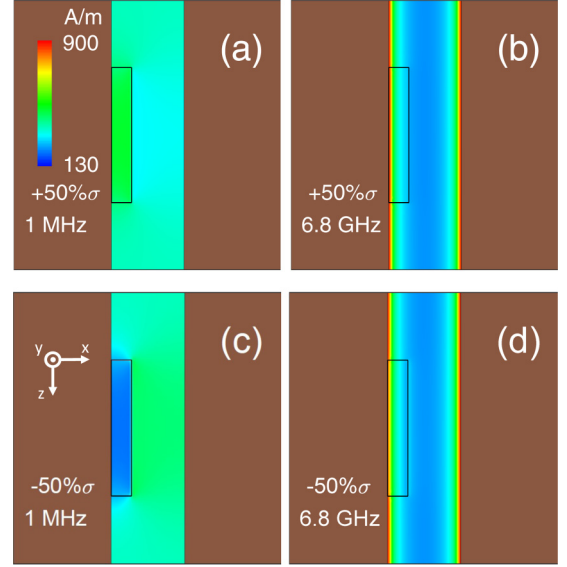


FIG. 11. Current distribution in a copper microstrip due to an unusually large $\pm 50\%$ conductivity patch defect. The microstrip is nominally 50 Ω and driven with 20 mW of power at 1 MHz or 6.8 GHz. The performance at 1 MHz is representative of the current distribution for a dc current. (a) Low-frequency current distribution for a +50% conductivity patch. (b) High-frequency current distribution for a +50% conductivity patch. (c) Low-frequency current distribution for a -50% conductivity patch. (d) High-frequency current distribution for a -50% conductivity patch.

A. Conductivity-patch model

In this section, we model the current flow and the resulting magnetic near field due to a local conductivity variation, i.e., a “conductivity patch.” In particular, we focus on how the current flow and magnetic near field vary as a function of frequency.

At dc and low frequencies, current flows according to Ohm’s law. However, for an ac current, the ac skin effect redistributes the current towards the edges of a wire trace [33]. In the presence of a local conductivity variation defect, this ac skin effect competes with Ohm’s law to determine the current distribution in the trace. For illustrative effect, Fig. 11 shows the current distribution for a rectangular patch with an unusually large $\pm 50\%$ conductivity change at both high and low frequencies. At low frequency, the current distribution is dominated by Ohm’s law, resulting in a patch that effectively repulses [low conductivity, Fig. 11(a)] or attracts currents [high conductivity, Fig. 11(c)]. At very high frequencies, the ac skin effect modifies the current distribution significantly and pushes the current to the trace edges, while also making the currents along the two edges more symmetric [Figs. 11(b) and 11(d)]. In turn, these changes in the current distribution affect the magnetic-field roughness and the trapping-potential roughness.

More specifically, we can determine how a current deviation, due to a conductivity patch, varies as a function of frequency. The center of current (COC) represents the average transverse current deviation. In terms of the parameters of the 1D wire model of Sec. IV, the COC is equivalent to the transverse deviation w of the wire current. The current

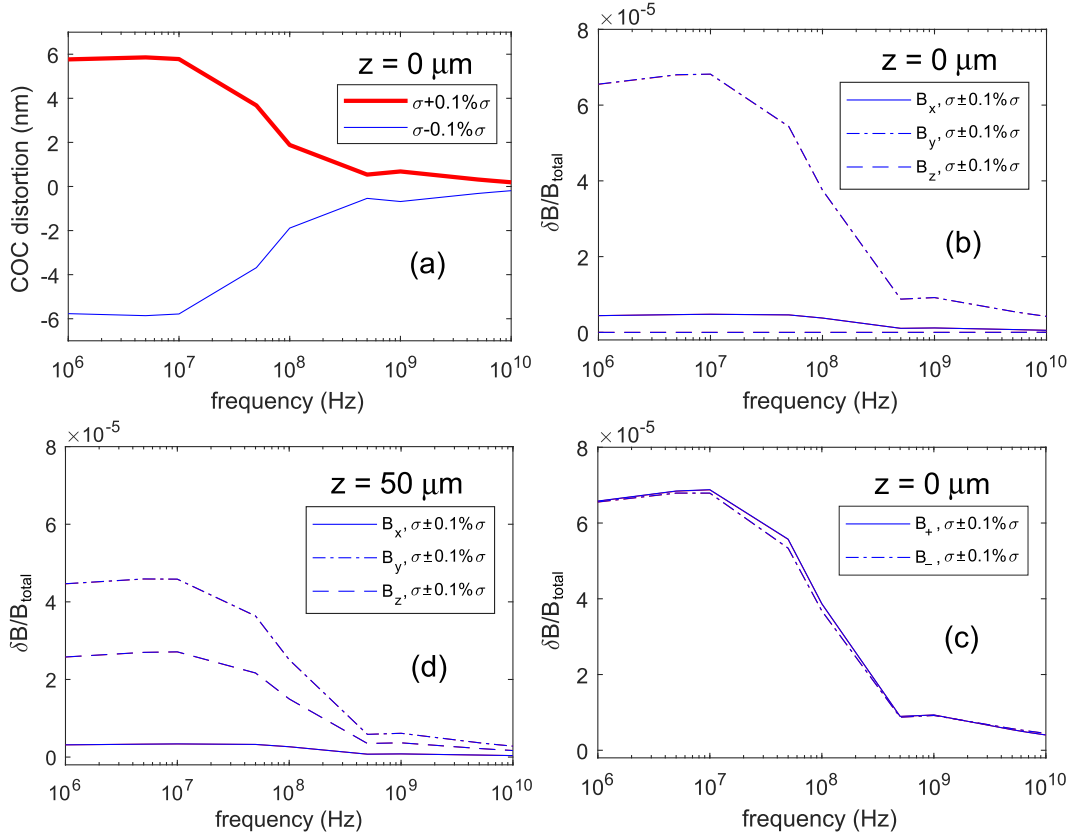


FIG. 12. Current and magnetic-field distortions due to the $\pm 0.1\%$ conductivity patch. (a) Center-of-current (COC) deviation along x axis, evaluated halfway down the length of the microstrip at $z = 0$. In the case of no conductivity patch, the COC is zero. The magnetic distortion δB is computed at the trap location, which is $100 \mu\text{m}$ above the geometric center of the trace. (b) The magnetic distortion $\delta B_{(x,y,z)}$ of the linearly polarized magnetic-field components at $z = 0$. (c) The magnetic distortion δB_{\pm} of the circularly polarized magnetic-field components at $z = 0$. (d) The distortion $\delta B_{(x,y,z)}$ of the magnetic-field components at $z = 50 \mu\text{m}$ (edge of conductivity patch). The $\sigma + 0.1\%\sigma$ and $\sigma - 0.1\%\sigma$ cases are indistinguishable at the resolution of plots (b)–(d) and so are plotted as a single curve.

deviation, in turn, generates a corresponding deviation in the ac magnetic near field at the location of the trap, which we take to be located at $h = 100 \mu\text{m}$ above the wire trace center.

We use a rectangular conductivity patch, shown in Fig. 10(b), based on the parameters of Table I and Ref. [27]. The patch has a conductivity variation of $\pm 0.1\%$, which accounts for actual conductivity variations or an equivalent change in the thickness of the trace over the patch area [27]. By placing the patch on one edge of the trace, the resulting COC deviation is maximized. The patch is located midway along the length of trace. We set the patch length at $l = 100 \mu\text{m}$ and then use a simulation at low frequency (1 MHz), with negligible skin effect, to determine the patch width that results in a transverse COC deviation of roughly 5 nm [see Fig. 5(a)], consistent with Table I: we settle on a patch width of $15 \mu\text{m}$, which results in a COC of $\delta x = 5.7 \text{ nm}$.

Formally, the COC is the average x -axis position of the surface current-density magnitude $K(x)$ (in A/m), i.e., $\text{COC} = \int K(x)x dx / \int K(x) dx$, where the integrals are taken over the $54 \mu\text{m}$ width of the microstrip trace. In practice, extracting a sufficiently smooth surface current density $K(x)$ from the simulation software is difficult given the triangular mesh, so instead we use the surface magnetic field $B_x(x)$ evaluated just 20 nm above the surface of the trace. In very

close vicinity of the surface current, the surface magnetic field (in the \hat{x} direction) is a good proxy for $K(x)$ since the two are related by $B_x(x) \simeq \mu_0 K(x)/2$ [33]. This relation is accurate as long as $B_x(x)$ is evaluated at a distance much closer than the characteristic length scale for spatial variations of $K(x)$, e.g., the skin depth or a local defect.

Figure 12(a) shows the COC due to the conductivity patch, evaluated halfway down the length of the microstrip trace at $z = 0$. The current distribution shifts towards the patch for a higher-conductivity patch ($\sigma + 0.1\%\sigma$ case) and shifts away from the patch for a lower-conductivity patch ($\sigma - 0.1\%\sigma$ case). In the two cases, the COC deviations are essentially equal and opposite. Importantly, the magnitude of the COC deviation remains constant at about 6 nm up to 10 MHz, after which it decreases steadily by roughly an order of magnitude as the frequency increases up to 1 GHz. From 1 GHz to 10 GHz, this decrease continues, but at a lower rate. For example, the COC deviation at 6.8 GHz is roughly 20 times smaller than at 10 MHz. The main conclusion for the COC plot in Fig. 12(a) is that current deviations due to conductivity variations are suppressed at high frequencies, potentially by an order of magnitude or more.

The current deviation of the conductivity patch also generates a distortion of the ac magnetic near field. We define this distortion as the difference δB between the magnetic near field

$B_{k,\text{defect}}$ (with $k = x, y, z$) with the conductivity of the patch set at $\sigma \pm 0.1\%\sigma$ and the magnetic near field $B_{k,\text{no-defect}}$ with the conductivity set to σ :

$$\delta B_k = |\tilde{B}_{k,\text{defect}} - \tilde{B}_{k,\text{no-defect}}|. \quad (12)$$

We use a tilde to denote a complex quantity, such as \tilde{B} , which incorporates magnitude and phase distortions associated with the conductivity patch. Importantly, we use the same computation mesh for simulating $\tilde{B}_{k,\text{defect}}$ and $\tilde{B}_{k,\text{no-defect}}$.

Since the hyperfine transitions used for ACZ trapping require circularly polarized magnetic fields, we also compute the magnetic distortion δB_{\pm} associated with the B_{\pm} components:

$$\delta B_{\pm} = |\tilde{B}_{\pm,\text{defect}} - \tilde{B}_{\pm,\text{no-defect}}|. \quad (13)$$

The complex \tilde{B}_{\pm} circular polarization components are computed according to the expressions

$$\tilde{B}_{\pm,\text{defect}} = \tilde{B}_{x,\text{defect}} \pm i\tilde{B}_{y,\text{defect}}, \quad (14)$$

$$\tilde{B}_{\pm,\text{no-defect}} = \tilde{B}_{x,\text{no-defect}} \pm i\tilde{B}_{y,\text{no-defect}}. \quad (15)$$

The magnetic distortion δB is evaluated at a trap height of $h = 100 \mu\text{m}$ above the geometric center of the trace (i.e., centered on the length and width of trace). For simplicity, the external magnetic field $B_{\text{ext-ac}}$ and the Ioffe field B_{Ioffe} are not included.

We compute the fractional distortion $\delta B/B_{\text{total}}$ using the total magnetic field B_{total} (undistorted):

$$B_{\text{total}} = \sqrt{\sum_{k=x,y,z} |\tilde{B}_{k,\text{no-defect}}|^2}. \quad (16)$$

Figures 12(b)–12(d) show that the fractional distortion $\delta B/B_{\text{total}}$ of the magnetic near field is suppressed at high frequencies above 10 MHz, with a falloff similar to that for the COC in Fig. 12(a). Consequently, potential roughness from bulk conductivity variations is suppressed by using high-frequency currents.

Figure 12(b) shows the magnetic distortion for a trap located halfway down the microstrip trace, i.e., at the middle of the conductivity path ($z = 0$). At this position, $\delta B_z = 0$ due to symmetry (i.e., $z = 0$ is located midway along the patch length). Furthermore, the B_y component of the magnetic near field has a much larger distortion than the B_x component, which is consistent with a small translation δx of the COC: In a simplified picture where all the current is at the COC (1D wire model), then from geometric projection we expect $\delta B_y/B_x = \delta x/h$ and $\delta B_x/B_x = (1/2)(\delta x/h)^2$, with $B_{\text{total}} \simeq B_x$. At low frequency, we have $\delta x \simeq 5.7 \text{ nm}$ for the COC at 1 MHz, so for $h = 100 \mu\text{m}$, we expect $\delta B_y/B_{\text{total}} = 5.7 \times 10^{-5}$, which is roughly consistent with $\delta B_y/B_{\text{total}} = 6.5 \times 10^{-5}$ in the plot of Fig. 12(b) at 1 MHz.

At high frequency (i.e., 10 GHz), the y -axis distortion $\delta B_y/B_{\text{total}}$ in Fig. 12(b) is somewhat larger than expected from the COC result: The COC has a deviation of about $\delta x = 0.25 \text{ nm}$, which corresponds to a fractional magnetic distortion of 2.5×10^{-6} , but $\delta B_y/B_{\text{total}} \simeq 4 \times 10^{-6}$. The simulation gives a magnetic distortion 60% larger than expected from a simple model where all the current is located at the COC, thus

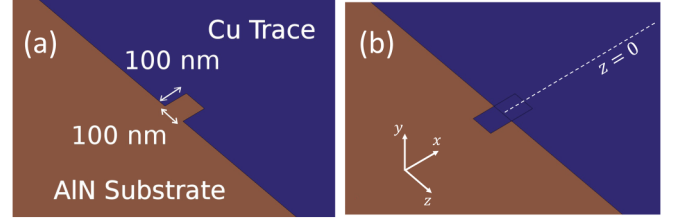


FIG. 13. Microstrip edge-defect models. The edge defect consist of a square with a 100 nm side that is either missing or that protrudes from the conducting trace's edge. (a) Defect-in model. (b) Defect-out model. The defect is located midway down the length of the trace at $z = 0$. Due to the very small size of the edge defect, we use a finer computation mesh within it (and in its vicinity) with triangles on the order of 20 nm in size.

showing that the full current distribution must be taken into account.

Figure 12(c) shows that the conductivity patch does not just modify the magnitude of the current distribution but also the phase. The plot shows that the δB_+ and δB_- components [given by Eqs. (13)–(15)] are similar but not identical in magnitude, thus indicating that the B_x and B_y components have accumulated a small phase difference between them due to the conductivity patch.

Finally, Fig. 12(d) shows the magnetic distortion at the edge of the conductivity patch ($z = 50 \mu\text{m}$). In this case, the longitudinal magnetic distortion δB_z is nonzero and also follows the trend of suppressed roughness at high frequencies. At low frequency (1 MHz), $\delta B_z/B_{\text{total}} = 2.6 \times 10^{-5}$ is roughly consistent with the performance observed for the 1D wire model with $w = 5 \text{ nm}$. Indeed, Fig. 5(a) shows a DCZ trapping potential deviation of 20 nK, which corresponds to a fractional deviation of $\delta B_z/B_{\text{total}} \simeq 1.7 \times 10^{-5}$ (or 1.9×10^{-5} when adjusted for a COC deviation of $\delta x = w \simeq 5.7 \text{ nm}$).

B. Edge-defect model

In this section, we show that an ac current experiences a larger deviation from a localized defect in the sidewall of a trace than a dc current. The ac skin effect concentrates the current along the inside edges of the microstrip, thus making the current distribution more susceptible to defects in the trace edges, i.e., edge defects. Furthermore, we find that an edge defect in which material is missing from the sidewall, referred to as “defect in,” has a larger impact on the ac current path than a defect where the sidewall sticks out, referred to as “defect out.” However, this high-frequency ac roughness due to sidewall imperfections is only about a factor of two larger than the dc case, for edge defects based on Table I. At high frequency (10 GHz), a defect in generates a COC deviation that is comparable in magnitude to that from the conductivity patch.

We study the effect of edge defects on the current path and the magnetic near field roughness with the simple edge defect model shown in Fig. 13. A $100 \text{ nm} \times 100 \text{ nm}$ square conducting patch is either added to the sidewall of the trace (i.e., defect out) or removed from it (i.e., defect in). Figure 14 shows the current density in the vicinity of the edge defect at low frequency (1 MHz) and high frequency (6.8 GHz). In the case of a defect-in, the current cannot enter the area

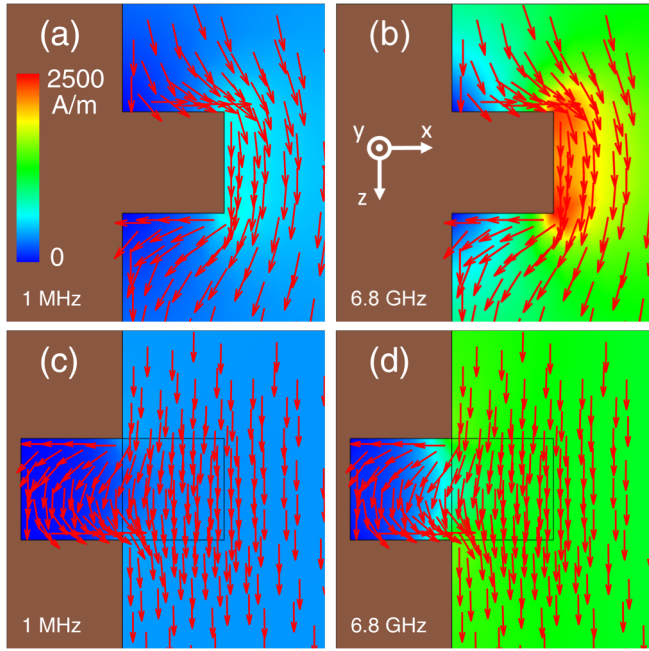


FIG. 14. Current distribution in the vicinity of an edge defect for a microstrip trace. (a) Defect-in model at low frequency (1 MHz), which is representative of dc performance. (b) Defect-in model at high frequency (6.8 GHz). (c) Defect-out model at low frequency (1 MHz). (d) Defect-out model at high frequency (6.8 GHz). The color bar shows the magnitude of the current density and is the same for all four panels. The arrows show the direction of the current-density magnitude. Displacement currents are not shown.

of missing conductor, and so the current experiences a fairly significant disruption to its average path. In the case of a defect-out, the current does enter the conducting protrusion, but not significantly so, and thus the current experiences a much smaller deviation. However, in both of these cases, the ac skin effect ensures a larger current deviation at high frequency than at low frequency: at higher frequency, the current becomes increasingly concentrated on the lateral edges of the trace, leading to a larger fraction of the current that can be deviated by an edge defect.

We evaluate the COC by the same method used for the conductivity patch. The COC is the average transverse shift δx in the microstrip current due to the edge defect, and it represents the current deviation width parameter w in the 1D wire model. Figures 15(a) and 15(b) show that the COC shifts away from a defect-in and towards a defect-out, as expected. This shift increases by a factor of two from dc to 10 GHz. The largest shift is for the defect-in case, which varies from 1 to 2 nm: this COC shift is larger than the one generated by the conductivity patch above 100 MHz [see Fig. 12(a)], albeit over a much shorter axial length. In contrast, the COC shift for the defect-out case is more than an order of magnitude smaller and varies from 40 to 80 pm (factor of ≈ 25 smaller).

We calculate the distortion of the magnetic field δB due to an edge defect with the same method as for the conductivity patch model, i.e., using Eqs. (13)–(16). Figures 15(c)–15(f) shows the magnetic-field distortion for edge defects as a function of frequency. Similar to the COC deviation, the defect-in generates a magnetic-field distortion that is over an

order of magnitude larger (factor of ≈ 25) than the defect-out. At higher frequencies, the magnetic distortion generally increases: the δB_x distortion increases by a factor of two to three from 1 MHz to 10 GHz, while the larger δB_y distortion sees only a modest increase over this frequency range. The longitudinal magnetic field B_z should be null by symmetry, and indeed δB_x is negligible at low frequencies. However, for frequencies above 1 GHz, δB_z develops a nonzero value (mechanism not investigated) and becomes comparable to δB_x (albeit smaller) at frequencies above 1 GHz.

Similar to the conductivity patch model, the \hat{y} component of the magnetic field experiences the largest distortion from the edge defects, while the \hat{x} component distortion is generally 2–10 times smaller. However, in comparison with the conductivity patch model, the edge defects generate a magnetic-field distortion that is typically an order of magnitude or more smaller at low frequencies. For example, at 1 MHz the conductivity patch generates a δB distortion that is 30 times larger than the largest edge-defect distortion (defect-in). However, at high frequencies, the conductivity patch and edge defect distortions become comparable, even though the edge defect is more than three orders of magnitude smaller in size than the conductivity patch: at 10 GHz, the COC deviation for the defect-in is somewhat larger than the conductivity patch COC deviation, while the magnetic-field distortion for the conductivity patch is only two times larger than the defect-in distortion.

Finally, at high frequencies, the edge defect induces a phase difference between the x and y magnetic components, thus leading to different B_+ and B_- circular polarization components of the near field. This effect is most apparent in the case of the defect-out above 1 GHz, which is clearly visible in Fig. 15(f).

VI. SUMMARY AND OUTLOOK

In summary, we have shown that potential roughness for an ACZ chip trap is expected to be strongly suppressed relative to a similar DCZ chip trap. The character of the roughness differs between the two traps. In a DCZ trap, the roughness primarily modifies the local strength of the potential at the bottom of the trap due to a magnetic-field component along the wire axis. In an ACZ trap, the roughness manifests itself primarily as a small local shift in the transverse location of the trap in the plane parallel to the chip.

The roughness suppression is due to two main mechanism: (1) Roughness in the ac magnetic near field contributes only modestly to the ACZ trapping potential since it tends to drive transitions that are not allowed by selection rules or that are suppressed because they are far off resonance; and (2) at high frequencies, the ac skin effect suppresses current deviations due to bulk conductivity variations in the chip wires. Table II summarizes the suppression of roughness for ACZ traps operating at low and high frequencies due to these two effects. Furthermore, multiple defects tend to smoothen out the roughness from any one defect, thus resulting in further suppression of ACZ potential roughness. However, we also find that at high frequencies the ac skin effect leads to a small increase in roughness (factor of two or less) due to defects in the edges of a chip wire trace.

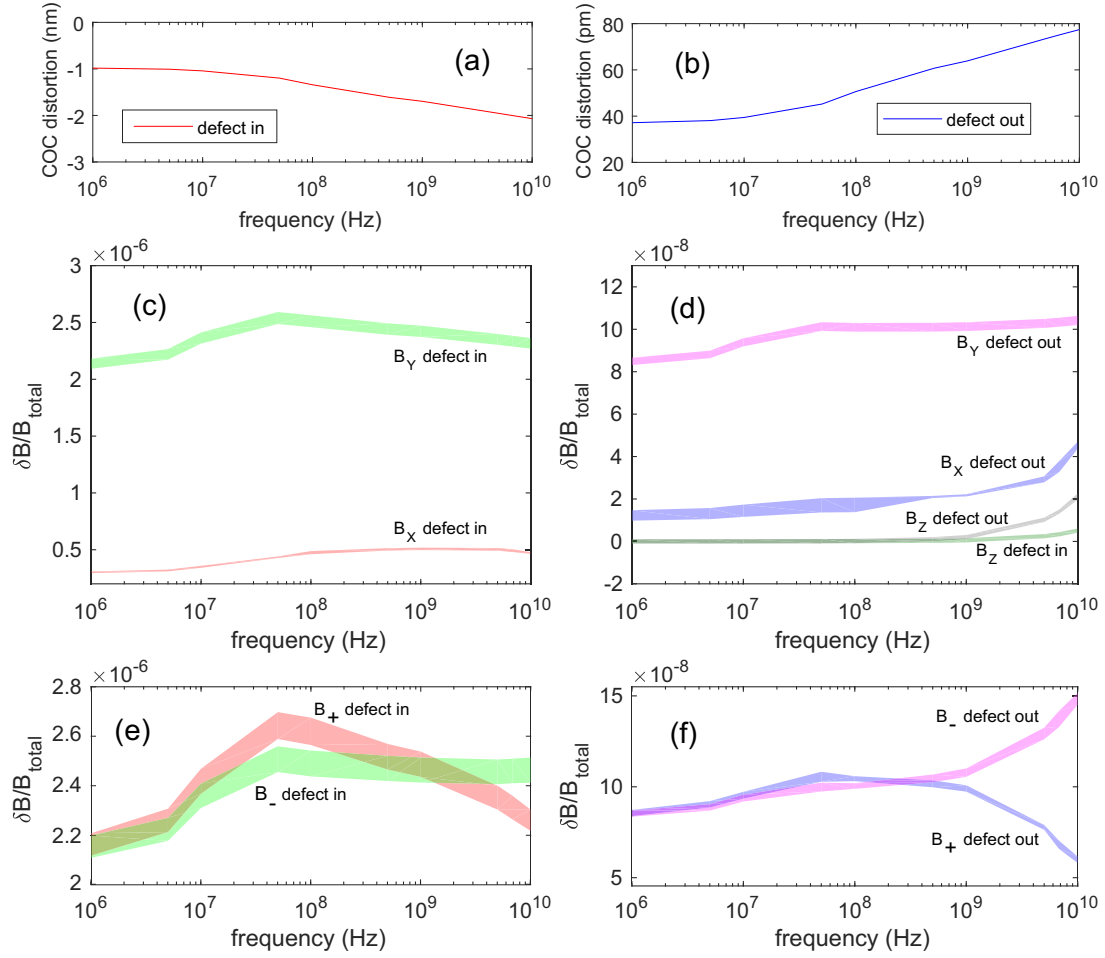


FIG. 15. Current and magnetic-field distortions due to “in” and “out” edge defects. The defect is located at $z = 0$. (a) Center-of-current (COC) deviation for the defect-in. (b) COC deviation for the defect-out. The COC deviation is along the x axis passing through the center of the edge defect. The magnetic distortion δB is computed at the trap location, which is $100 \mu\text{m}$ above the geometric center of the trace and at $z = 0$. (c) The magnetic distortion $\delta B_{(x,y)}$ of the linearly polarized magnetic near field components for the defect-in. (d) The magnetic distortion $\delta B_{(x,y,z)}$ for the defect-out, as well as δB_z for the defect-in. (e) The magnetic distortion δB_{\pm} of the circularly polarized magnetic-field components for the defect in. (f) The magnetic distortion δB_{\pm} for the defect-out. For panels (c)–(f), we use ribbons to show the max-min range of values obtained from multiple simulations with different mesh layouts in the vicinity of the edge defect.

TABLE II. Summary of roughness suppression for an ACZ trap, relative to a comparable DCZ trap, located at a distance $h = 100 \mu\text{m}$ from the chip wire. The roughness is generated by a single current deviation with dc parameters $w = 5 \text{ nm}$ and $l = 100 \mu\text{m}$, due to a bulk conductivity variation of $\pm 0.1\%$. The suppression factor contributions are based on Fig. 5(a), the $1/w$ scaling in Figs. 9(b) and 12(a).

Suppression mechanism	Suppression factor contribution	
	rf trap 10 MHz	Microwave trap 6.8 GHz
ACZ physics (Secs. III–IV)	2×10^4	2×10^4
ac skin effect, cond. patch (Sec. V A, COC deviation)	1	20
Combined suppression	2×10^4	4×10^5

While the increase in current deviations due to edge defects is small, it becomes comparable to deviations due to bulk conductivity variations at high frequency (1 GHz and above). However, the short length of edge defects ($\approx 100 \text{ nm}$) limits the resulting roughness of traps that are sufficiently far from the chip. Furthermore, edge defects are easier to observe and correct in the chip manufacturing process, since they can be observed by visual inspection, unlike bulk-conductivity variations.

We note that the microstrip transmission line approach to ACZ trapping opens up two new sources of roughness that are not studied in this paper. Defects in both the dielectric substrate and the ground plane could contribute to the potential roughness in a microwave ACZ trap. These roughness mechanisms are a topic for future research and have no analog in DCZ chip traps.

We recall that the roughness of the ACZ potential in this paper is based on a simplified two-level model of the atom’s hyperfine ground states. A more accurate treatment

should include the role of far-off-resonance transitions (e.g., π transition), which can result in a small ACZ energy shift of the untrapped state [i.e., $|g\rangle$ in Fig. 2(b)]. This small level shift will then generate a roughness-induced, position-dependent shift of the detuning $\delta(z)$ on the $|e\rangle \leftrightarrow |g\rangle$ trapping transition. In this way, current deviations can drive far-off-resonance transitions, which can exacerbate the ACZ potential roughness, although this contribution is suppressed by the far-off-resonance nature of the transitions. This roughness mechanism depends on the atom's specific hyperfine structure, the DCZ energy shifts from the axial magnetic field B_{Ioffe} , and the detuning δ and is a topic for future, more detailed theoretical work.

To conduct an experimental verification of roughness suppression, the DCZ and ACZ traps must be generated from the same source wires. A chip with three parallel wires generates a trap without the need for an externally applied magnetic field B_{ext} , as the two outer wires generate B_{ext} on-chip. These wires can support dc or rf currents, and so the same three wires can generate an ACZ trap or a comparable DCZ trap. In the case of a microwave ACZ trap, the three wires must be replaced by microstrips [25], which can also support dc currents.

A qualitative observation of roughness suppression can be conducted by the same method used in Ref. [11,36], whereby the trapping potential and its roughness are extracted from *in situ* images of the atomic density profile. In the case of chip traces with current deviations consistent with the parameters of Table I, the DCZ trap roughness can be observed with a thermal gas with a temperature of 10–100 nK or a BEC. However, the ACZ roughness is expected to be in the pK range [see Fig. 5(a)], which is too small to be observable with

this method. Such an experiment will only provide a qualitative observation of roughness suppression, unless another roughness mechanism exists beyond those considered in this paper. To measure both DCZ and ACZ roughness, the simplest method is to use an unusually large defect (e.g., an engineered artificial defect), such as the one in Fig. 5(b).

If the predictions for the suppression roughness are confirmed by experiment, then an ACZ trap can be operated closer to the chip traces without suffering from significant roughness. Operating closer to the chip will result in lower microwave power requirements, and will also benefit from steeper and deeper trapping potentials. In an atomtronics context, operation closer to the chip can be done with narrower traces for denser integration. In a physics context, operation closer to the chip also opens up the possibility of using other potentials for manipulating atoms, such as the ac Stark potential generated by a microwave electric near field and eventually evanescent optical fields. Looking forward, the ac Stark potential of a microwave near field will also include roughness and so is an avenue for future investigation.

ACKNOWLEDGMENTS

This work was supported by NSF Grant PHY-1806558, DTRA Grant HDTRA1-19-1-0027, and the College of William and Mary. The authors acknowledge William & Mary Research Computing for providing computational resources that have contributed to results in this paper. The authors thank J. Field for preliminary discussions on ACZ trapping and A. P. Rotunno for discussions and assistance with the ac skin effect.

-
- [1] J. Fortágh and C. Zimmermann, *Rev. Mod. Phys.* **79**, 235 (2007).
 - [2] W. Hänsel, P. Hommelhoff, T. W. Hänsch, and J. Reichel, *Nature (London)* **413**, 498 (2001).
 - [3] S. Aubin, S. Myrskog, M. H. T. Extavour, L. J. LeBlanc, D. McKay, A. Stummer, and J. H. Thywissen, *Nat. Phys.* **2**, 384 (2006).
 - [4] J. Estève, J.-B. Trebbia, T. Schumm, A. Aspect, C. I. Westbrook, and I. Bouchoule, *Phys. Rev. Lett.* **96**, 130403 (2006).
 - [5] Y.-J. Wang, D. Z. Anderson, V. M. Bright, E. A. Cornell, Q. Diot, T. Kishimoto, M. Prentiss, R. A. Saravanan, S. R. Segal, and S. Wu, *Phys. Rev. Lett.* **94**, 090405 (2005).
 - [6] T. Schumm, S. Hofferberth, L. M. Andersson, S. Wildermuth, S. Groth, I. Bar-Joseph, J. Schmiedmayer, and P. Krüger, *Nat. Phys.* **1**, 57 (2005).
 - [7] P. Böhi, M. F. Riedel, J. Hoffrogge, J. Reichel, T. W. Hänsch, and P. Treutlein, *Nat. Phys.* **5**, 592 (2009).
 - [8] Y.-J. Lin, I. Teper, C. Chin, and V. Vuletić, *Phys. Rev. Lett.* **92**, 050404 (2004).
 - [9] E. R. Elliot, M. C. Krutzik, J. R. Williams, R. J. Thompson, and D. C. Aveline, *npj Microgravity* **4**, 16 (2018).
 - [10] S. C. Caliga, C. J. E. Straatsma, and D. Z. Anderson, *New J. Phys.* **18**, 025010 (2016).
 - [11] P. Krüger, L. M. Andersson, S. Wildermuth, S. Hofferberth, E. Haller, S. Aigner, S. Groth, I. Bar-Joseph, and J. Schmiedmayer, *Phys. Rev. A* **76**, 063621 (2007).
 - [12] A. E. Leanhardt, A. P. Chikkatur, D. Kielpinski, Y. Shin, T. L. Gustavson, W. Ketterle, and D. E. Pritchard, *Phys. Rev. Lett.* **89**, 040401 (2002).
 - [13] Y. Shin, C. Sanner, G.-B. Jo, T. A. Pasquini, M. Saba, W. Ketterle, D. E. Pritchard, M. Vengalattore, and M. Prentiss, *Phys. Rev. A* **72**, 021604(R) (2005).
 - [14] S. Groth, P. Krüger, S. Wildermuth, R. Folman, T. Fernholz, J. Schmiedmayer, D. Mahalu, and I. Bar-Joseph, *Appl. Phys. Lett.* **85**, 2980 (2004).
 - [15] J.-B. Trebbia, C. L. Garrido Alzar, R. Cornelussen, C. I. Westbrook, and I. Bouchoule, *Phys. Rev. Lett.* **98**, 263201 (2007).
 - [16] K. Wongcharoenbhorn, R. Crawford, N. Welch, F. Wang, G. Sinuco-León, P. Krüger, F. Intravaia, C. Koller, and T. M. Fromhold, *Phys. Rev. A* **104**, 053108 (2021).
 - [17] C. C. Agosta, I. F. Silvera, H. T. C. Stoof, and B. J. Verhaar, *Phys. Rev. Lett.* **62**, 2361 (1989).
 - [18] R. J. C. Spreeuw, C. Gerz, L. S. Goldner, W. D. Phillips, S. L. Rolston, C. I. Westbrook, M. W. Reynolds, and I. F. Silvera, *Phys. Rev. Lett.* **72**, 3162 (1994).

- [19] A. P. Rotunno, W. Miyahira, S. Du, and S. Aubin (unpublished); A. P. Rotunno, S. Du, W. Miyahira, and S. Aubin, Radio frequency ac Zeeman trapping on an atom chip, talk H09.00007, DAMOP 2021 conference (on-line).
- [20] C. T. Fancher, A. J. Pyle, A. P. Rotunno, and S. Aubin, *Phys. Rev. A* **97**, 043430 (2018).
- [21] A. P. Rotunno, S. Du, and S. Aubin (unpublished).
- [22] M. Ammar, M. Dupont-Nivet, L. Huet, J.-P. Pocholle, P. Rosenbusch, I. Bouchoule, C. I. Westbrook, J. Estève, J. Reichel, C. Guerlin, and S. Schwartz, *Phys. Rev. A* **91**, 053623 (2015).
- [23] V. Guarrera, R. Szmuk, J. Reichel, and P. Rosenbusch, *New J. Phys.* **17**, 083022 (2015).
- [24] The Landé g factor is given by $g_F = [F(F + 1) - S(S + 1) - I(I + 1)]/[F(F + 1)]$, where F is the total angular momentum of the atom, I is the nuclear spin, and $S = 1/2$ is the electron's spin.
- [25] W. Miyahira, A. P. Rotunno, S. Du, and S. Aubin, *Atoms* **9**, 54 (2021).
- [26] J. H. Thywissen, M. Olshanii, G. Zabow, M. Drndić, R. M. Westervelt, and M. Prentiss, *Eur. Phys. J. D* **7**, 361 (1999).
- [27] S. Aigner, L. D. Pietra, Y. Japha, O. Entin-Wohlman, T. David, R. Salem, R. Folman, and J. Schmiedmayer, *Science* **319**, 1226 (2008).
- [28] M. A. Schneider, M. Wenderoth, A. J. Heinrich, M. A. Rosentreter, and R. G. Ulbrich, *Appl. Phys. Lett.* **69**, 1327 (1996).
- [29] O. Cherry, J. D. Carter, and J. D. D. Martin, *Can. J. Phys.* **87**, 633 (2009).
- [30] Y. Japha, O. Entin-Wohlman, T. David, R. Salem, S. Aigner, J. Schmiedmayer, and R. Folman, *Phys. Rev. B* **77**, 201407(R) (2008).
- [31] T. Schumm, J. Estève, C. Figl, J.-B. Trebbia, C. Aussibal, H. Nguyen, D. Mailly, I. Bouchoule, C. I. Westbrook, and A. Aspect, *Eur. Phys. J. D* **32**, 171 (2005).
- [32] R. B. Firestone, V. S. Shirley, C. M. Baglin, S. Y. F. Chu, and J. Zipkin, *Table of Isotopes*, 8th ed. (John Wiley & Sons, New York, 1996).
- [33] A. E. Blackwell, A. P. Rotunno, and S. Aubin, *Am. J. Phys.* **88**, 676 (2020).
- [34] R. E. Collin, *Foundations for Microwave Engineering*, 2nd ed. (John Wiley & Sons, Hoboken, 2001).
- [35] The FEKO-based results presented in these two sections represent about 3500 hours of simulations on a high-performance computing cluster.
- [36] M. K. Ivory, A. R. Ziltz, C. T. Fancher, A. J. Pyle, A. Sensharma, B. Chase, J. P. Field, A. Garcia, D. Jervis, and S. Aubin, *Rev. Sci. Instrum.* **85**, 043102 (2014).